1 **Time varying changes and uncertainties in the CMIP6 ocean carbon sink from global to regional**

2 **to local scale**

3 Parsa Gooya[1], Neil C. Swart[2,1], Roberta C. Hamme[1]

4 [1]School of Earth and Ocean Sciences, University of Victoria, Victoria, BC, V8P 5C2, Canada

5 [2]Canadian Centre for Climate Modelling and Analysis, Environment and Climate Change Canada, Victoria, BC,

6 V8W 2P2, Canada

7 *Correspondence to*: Parsa Gooya (parsa.g76@gmail.com)

8 **Abstract.** As a major sink for anthropogenic carbon, the oceans slow the increase of carbon dioxide in the

9 atmosphere and regulate climate change. Future changes in the ocean carbon sink, and its uncertainty at a global

10 and regional scale, are key to understanding the future evolution of the climate. Here, we conduct a multimodel

11 analysis of the changes and uncertainties in the historical and future ocean carbon sink using output data from the

12 latest phase of the Coupled Model Intercomparison Project: CMIP6, and observations. We show that the ocean

13 carbon sink is concentrated in highly active regions - 70 percent of the total sink occurs in less than 40 percent of

14 the global ocean. High pattern correlations between the historical and projected future carbon sink indicate that

15 future uptake will largely continue to occur in historically important regions. We conduct a detailed breakdown of

16 the sources of uncertainty in the future carbon sink by region. Scenario uncertainty dominates at the global scale,

17 followed by model uncertainty, and then internal variability. We demonstrate how the importance of internal

18 variability increases moving to smaller spatial scales and go on to show how the breakdown between scenario,

19 model, and internal variability changes between different ocean basins, governed by different processes. Moreover,

20 we show that internal variability changes with time based on the scenario. As with the mean sink, we show that

21 uncertainty in the future ocean carbon sink is also concentrated in the known regions of historical uptake. The

22 resulting patterns in the signal-to-noise ratio have strong implications for observational detectability and time of

23 emergence, which varies both in space and with scenario. Our results suggest that to detect human influence on the

24 ocean carbon sink as early as possible, and to efficiently reduce uncertainty in future carbon uptake, modelling and

25 observational efforts should be focused in the known regions of high historical uptake, including the Northwest

26 Atlantic and the Southern Ocean.

1. Introduction

Recent increases in greenhouse gases have trapped additional heat relative to the pre-industrial era and raised Earth's average temperature. Carbon dioxide (CO_2) is the primary driver of the global warming in the industrial period (Masson-Delmotte et al., 2021). The concentration of atmospheric CO_2 has increased from approximately 277 parts per million (ppm) in 1750 (Joos et al., 2008), the beginning of the Industrial Era, to 409 ppm in 2019. However, less than half of the anthropogenic CO_2 has remained in the atmosphere; the remaining CO_2 has been taken up by the natural carbon sinks of the ocean and the terrestrial biosphere. Specifically, the global ocean absorbed ~26% of the total CO_2 emissions during 2011-2020 (Friedlingstein et al., 2021).

The ocean's capacity to absorb increasing amounts of anthropogenic CO_2 is not uniformly distributed (McKinley et al., 2016). Despite increasing atmospheric CO_2 concentrations, the air-sea CO_2 flux does not change much in the subtropical gyres. The regions where ocean carbon uptake notably increases are those with strong exchange between the surface and the deep ocean (McKinley et al., 2016). Even within regions there are large variations in the sink. The Northeast Pacific, for instance, is a net sink for atmospheric CO_2. However, the region includes diverse oceanographic areas such as open ocean, continental margins, and fjords, leading to large spatial variability in the direction of the CO_2 sea-air flux (Sutton et al., 2017; Takahashi et al., 2006). In the Southern Ocean, the spatial superposition of natural and anthropogenic CO_2 fluxes leads to a relatively strong uptake band between approximately 55°S and 35°S (Gruber et al., 2019). However, south of the Polar Front (55°S), the different estimates agree less well (Gruber et al., 2019). Supported by measurements based on biogeochemical floats (Gray et al., 2018; Williams et al., 2018), Gruber et al. (2019) argues that the region was most likely a small source in 2019.

Earth System Models (ESMs) are the primary tool for projecting the future evolution of ocean carbon uptake on subannual to centennial timescales. However, quantitative projections from ESMs across these timescales are subject to considerable uncertainty, particularly at regional and local scales (Friedrich et al., 2012; Frölicher et al., 2014; Hauck et al., 2015; Laufkötter et al., 2015; Roy et al., 2011; Tjiputra et al., 2014) where less averaging is done and more diverse mechanisms dominate. Projection uncertainty varies with lead time, spatial averaging scale, and from region to region. For example, Lovenduski et al. (2016) showed a spatially heterogeneous pattern of projection uncertainty in CO_2 flux projections over 17 regions; at the scale of the California Current System, uncertainty was relatively higher compared to the global scale. If ESMs are to be used to quantify future changes

57 in ocean carbon uptake, especially across shorter timescales and at regional spatial scales, and to inform

58 observational campaign planning, their uncertainties must be well known and well understood (Lovenduski et al.,

59 2016).

60

61 A systematic characterization of projection uncertainty has become possible with the advent of the Coupled Model

62 Intercomparison Project (CMIP), as a number of climate models of similar complexity provided simulations over

63 a consistent time period and with the same set of emissions scenarios (Lehner et al., 2020). We consider three main

64 types of projection uncertainty, as described by Hawkins and Sutton (2009) (hereafter HS09):

65

66 **Uncertainty due to internal variability:** Internal variability is the unforced natural climate variability resulting

67 from the internal processes in the climate system. Modes such as the El Niño–Southern Oscillation, North Atlantic

68 Oscillation, Atlantic Multidecadal Oscillation, Pacific Decadal Oscillation, and Southern Annular Mode (SAM)

69 contribute, along with others, to this internal variability. The real world follows only one of an infinite possible

70 number of *realizations* of internal variability, and the future evolution of internal variability is not predictable

71 beyond short timescales. Climate model simulations do not attempt to reproduce the exact observed evolution of

72 internal variability, but produce their own, unique realizations that aim to capture the correct statistics of this

73 variability. Hence, our analysis must account for internal variability, both when comparing historical model

74 simulations to observations, and when considering uncertainties in the future ocean carbon sink. In HS09, a fourth-

75 order polynomial fit to simulated global and regional temperature timeseries represented the forced response, while

76 the residual from this fit represented the internal variability. However, this approach could possibly conflate internal

77 variability with the forced response in cases where low-frequency (decadal-to-multidecadal) internal variability

78 exists, or when the forced signal is weak, which makes the statistical fit a poor estimate of the forced response

79 (Kumar and Ganguly, 2018). In this study, we instead use a Single-Model Initial-condition Large

80 Ensemble (SMILE) to robustly quantify the simulated forced response and internal variability using ensemble

81 statistics (Lehner et al., 2020). A SMILE is an ensemble of model realizations that each starts from different initial

82 conditions but uses the same model and forcing, and provides representations of the climate system that are

83 equivalent except for internal variability.

84 **Uncertainty due to model structure:** Each model has a specific way of representing the physical world. Models

85 differ in their resolution, structure, numerics, and parameterization of processes. These differences cause models

86 to respond differently to the same forcing. For example, the CMIP5 model simulations run under Representative

87   Concentration Pathway 8.5 (RCP8.5) project a wide range of cumulative anthropogenic carbon storage by 2100

88   (320–635 Pg-C) (Ciais and Sabine, 2013) due to both internal variability and model uncertainty (Lovenduski et al.,

89   2016).

90   **Uncertainty due to emission scenario:** The future of the climate system depends on human activity and our

91   emission of climate active gases that change radiative forcing. Future emissions are highly uncertain, given our

92   inability to project the complex changes in society and technology upon which they depend. As a result, future

93   simulations are run with a range of possible "scenarios" for how future emissions (or atmospheric concentrations)

94   will evolve under different socioeconomic storylines. These scenarios are prescribed via the internationally

95   coordinated experiments organized by the Coupled Model Intercomparison Project. Since the future emission

96   trajectory is unknown, these future simulations are referred to as projections, rather than predictions. Projections

97   of future ocean carbon uptake from ESMs are greatly influenced by the choice of emission scenario (Lovenduski

98   et al., 2016). For example, the cumulative oceanic storage of anthropogenic carbon in CMIP5 models by 2100

99   ranges from 110–220 Pg-C under RCP2.6 to 320–635 Pg-C under RCP8.5 (Ciais and Sabine, 2013).

00   In this paper we start by analysing the regional patterns of historical ocean carbon uptake and how they are projected

01   to change in the future (Sect. 3.1). Then, we examine the partitioning among different sources of uncertainty (Sect.

02   3.2) and the scale dependence of this partitioning analysis (Sect. 3.3) to understand how the uncertainty and

03   distribution among sources differ based on scale of integration and region of interest (Sect. 3.4). The final section

04   explores the detectability of the model projected signal given the uncertainty imposed by internal variability, in

05   order to make useful suggestions for future observations.

06   **2. Data and Methods**

07   2.1 Model Data Selection

08   Here we use results from models selected from the 6th Coupled Model Intercomparison Project (CMIP6; Eyring et

09   al., 2016). Models are chosen based on availability, meaning all models that provided at least one realisation for

10   air-sea CO_2 flux (fgco2) for the experiments of interest. One realization of each model over the historical period

11   and three scenarios that represent the low (ssp126), mid (ssp245), and high (ssp585) ranges of future atmospheric

12   CO_2 concentrations are analysed. A total of 16 models met these criteria, out of which 3 were excluded as outliers

13   (see section S1 in the Supplements). To maintain equal sampling, only one realization of each model is selected,

14   except when specifically using the large ensembles to assess internal variability. Finally, since the ocean component

15   of the models may be on different grids, all model data are remapped to a regular one-by-one-degree grid.

17   2.2 Sources of uncertainty

18   Three sources of uncertainty are considered following the approach of HS09. Total uncertainty is composed of

19   internal, model, and scenario uncertainty in equation 1, which assumes that each of these sources is independent.

20   Here, each source of uncertainty is considered as a function of time (t) and location (l) (Lovenduski et al., 2016):

22    $$U_T{}^2(t,\ l) = U_I{}^2(t,\ l) + U_M{}^2(t,\ l) + U_s{}^2(t,\ l) \tag{1}$$

24   where $U_T(t,\ l)$ is total uncertainty, $U_I(t,\ l)$ is internal variability, $U_M(t,\ l)$ is model uncertainty, and $U_S(t,\ l)$ is

25   scenario uncertainty. The fractional uncertainties for each source are calculated as $\frac{U_I^2}{U_T^2}$, $\frac{U_M^2}{U_T^2}$, and $\frac{U_S^2}{U_T^2}$ (Lovenduski et

26   al., 2016).

27

28   HS09 assume $U_I(t,\ l)$ to be constant in time and use a 4th degree polynomial fit to measure internal variability as

29   the spread over time and scenario of the residuals for each models signal relative to the fitted signal. We show in

30   the Supplements (see section S2) that internal variability depends on time and scenario, so a better estimate of

31   internal variability should account for these variations. Here, we quantify internal variability as two times the

32   standard deviation of the annual carbon sink across many realizations from a Single Model Initial Condition Large-

33   ensemble based on CanESM5:

34

35

36    $$U_I(t,l) = 2\sqrt{\frac{1}{Ns}\sum_{s=1}^{N_S}\mathrm{Var\ (CanESM5\ Large\ Ensemble)}} \tag{2}$$

37

38   where s indicates each scenario (Ns is the number of scenarios) and Var indicates the variance over the large

39   ensemble of CanESM5. In the CanESM5 SMILE, each realization starts from different initial conditions which

40   are drawn from points separated by 50 years in the piControl simulation. Thus, the spread across the realizations

41 gives a robust estimate of the internal variability, including sampling over longer term ocean variability. Internal

42 variability is an important component of the uncertainty that is not reducible and results from the chaotic nature of

43 the climate system. Further details regarding the estimation of internal variability are explained in the Supplements

44 (see section S2). CanESM5 is the only model that has a large enough ensemble over the entire timeline and set of

45 experiments to make this estimate.

46

47

48 Model uncertainty is calculated by taking the variance across the forced signal of all available models for each

49 scenario, averaging over the three scenarios, and then reporting twice the square root of the result (Eq. 3).

50
$$U_M(t,l) = 2 \sqrt{\frac{1}{Ns} \sum_{s=1}^{N_s} \text{Var}_m\big(F(m,s,t,l)\big)} \qquad (3)$$

51 where Var_m means the variance taken across different models for individual times and scenarios, m indicates each

52 model, and t stands for time. $F(m,s,t,l)$ is the forced signal and can be related to each realization as follows:

53

54
$$T(m,s,t,l) = F(m,s,t,l) + R(m,s,t,l) \qquad (4)$$

55

56 Where, $T(m,s,t,l)$ represents the reported output, i.e. each realization, but must be corrected for internal

57 variability. $R(m,s,t,l)$ is the residual from the forced signal caused by internal variability. Here, the variance in

58 the forced signal across all models is calculated by correcting the total variance across each model realization for

59 the variance caused by internal variability. The corrections are done by subtracting the variance across the same

60 number of CanESM5 ensemble members as the multi-model ensemble (13 members) from the spread across one

61 realization of each of the 13 models. For this correction only, the sample sizes (13) are kept the same so that the

62 internal variability removed from the variance across the models' first realizations is not overestimated by a well

63 sampled 50-member ensemble (see section S3 in the Supplements).

64

65 U_s (t, l) is the scenario uncertainty. Scenario uncertainty is measured as twice the standard deviation (square root

66 of variance) across scenarios of the multi-model mean signal (Eq. 5).

67

68
$$U_S(t,l) = 2\sqrt{\text{Var}_m\left(\frac{1}{N_m}\sum_{m=1}^{N_m} T(m,s,t,l)\right)} \tag{5}$$

69 where N_m is the number of models. The multi-model mean across the first realizations of the 13 models gives the

70 multi-model forced response and does not require correction for internal variability as done for model uncertainty

71 before.

72

73 We conduct analysis on three different scales: single grid point (one-degree resolution), regional, and global. When

74 regional and global analysis is done, the dependence on location is taken away by integrating and averaging over

75 that region or the whole global ocean.

76

77 2.3 Time of Emergence

78 In order to know when the forced response is distinguishable from internal variability, time of emergence is

79 calculated following the approach of McKinley et al. (2016). The time of emergence is the first year when the

80 multi-model mean anomaly is larger than internal variability – two times the standard deviation across the 50

81 member CanESM5 ensemble - for five consecutive years (the first year of this five-year period is reported as the

82 time of emergence). The result is reported at each grid point for the 10-year running mean smoothed anomaly

83 relative to the 1995-2015 mean (detection of a change relative to the current state of the ocean).

84

85

86 2.4 Scale Dependence

87 Finally, the scale dependence of the sources of uncertainty is measured at year 2050 using ssp245 for internal

88 variability and model uncertainty, and using all scenarios for scenario uncertainty. The analysis is done by moving

89 a sliding sample window of a given area across the earth, and then repeating with a larger and larger window until

90 all scales from <100 km^2 to the whole Earth are considered. The average for all rectangles of the same ocean area

91 across the global ocean for each source of uncertainty is reported.

92

3. Results and Discussion

3.1 Global Analysis

The pattern of the carbon sink in the CMIP6 multi-model ensemble mean from the historical experiment over 1995-2015 matches that of the Landschützer (2016) Self Organizing Map - Feed Forward Neural Network (SOM-FFN) observation-based data product estimate (correlation coefficient of 0.84, compare Figs. 1a and 1b). We use the multi-model mean response to external forcing as a more robust estimate of the forced climate signal than the response of any single model (Tebaldi & Knutti, 2007). When compared to the observation-based data product, the CMIP6 multi-model mean shows a larger sink (positive flux) in the North Atlantic and North and North-West Pacific but a smaller sink in the Southern Ocean (Fig 1a, b). Additionally, the observation-based data product shows a larger source in the Equatorial Pacific and Indian Ocean than the CMIP6 multi-model ensemble.

While most of the global ocean shows a net sink relative to the pre-industrial era, the largest change takes place in regions such as the North Atlantic, Southern Ocean, Equatorial Pacific, and western boundary currents of the mid-latitude gyre systems in the Pacific and Atlantic Oceans (Fig. 1c). These regions of largest changes in the carbon sink seem to be the regions where there is a surface-depth connectivity. We refer to these regions as "hotspots" from here on. These results for CMIP6 are consistent with those for CMIP5 shown by McKinley et al. (2016).

The regions of largest future carbon uptake, relative to the 1995-2015 mean, are the same regions responsible for most of the uptake over the historical period. The correlation coefficients on top of each panel in Fig. 1 (except 1b) represent the correlation between future absolute anomalies, relative to 1995-2015, and anomalies in 1995-2015, relative to the pre-industrial era. The high correlations indicate that regions that have been most active in carbon sequestration since the pre-industrial era are the same regions that will continue to change most into the future, particularly with larger increases in atmospheric CO_2 (ssp585).
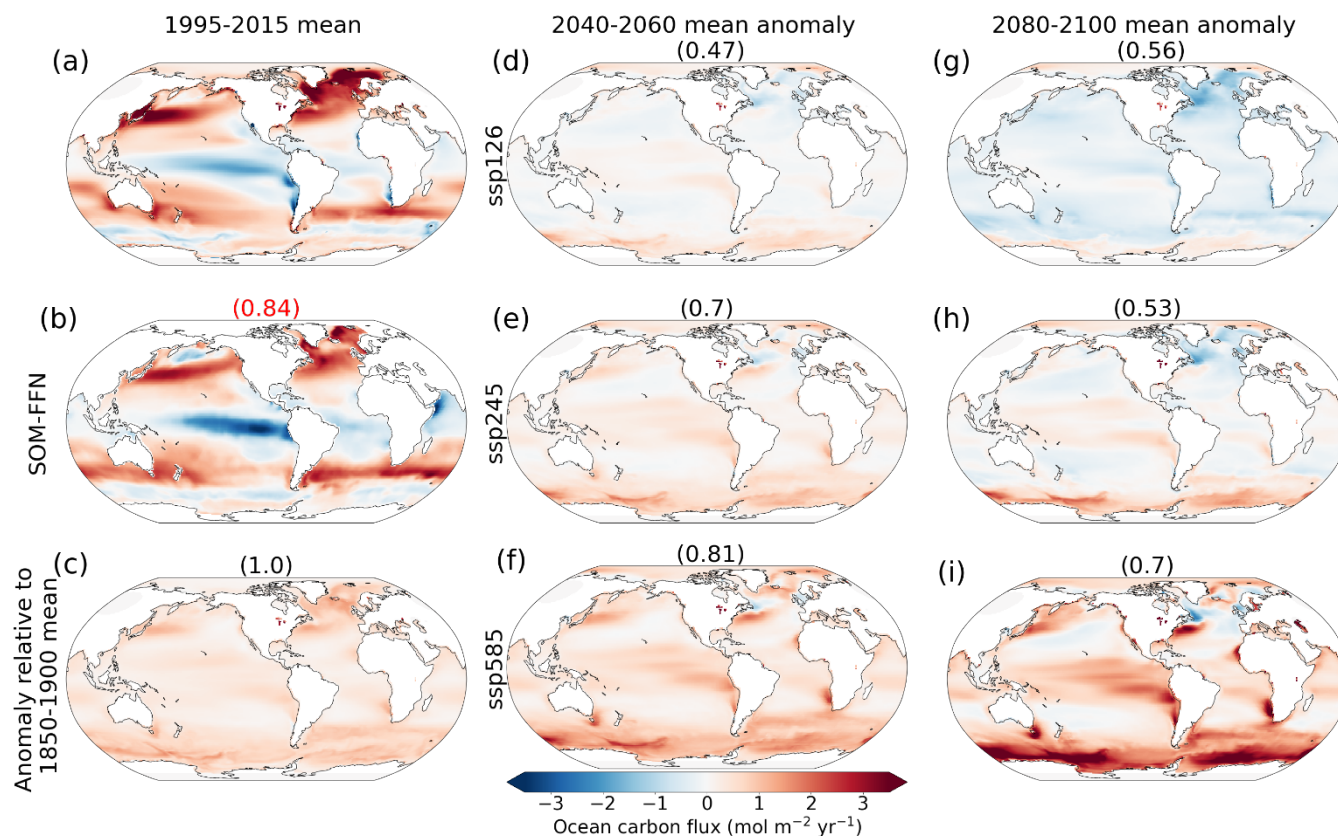
Figure 1- CMIP6 multi-model mean maps using one realization of each model. Columns represent different time periods,
being the recent time (1995-2015 mean), mid-century (2040-2060 mean), and late-century (2080-2100 mean). Note: the sink
is positive into the ocean. The first column shows (a) the carbon sink over 1995-2015, (b) Landschützer et al. (2016) SOM-
FFN product, and (c) the anomaly relative to the 1850-1900 mean. Other panels are anomalies relative to the 1995-2015
multi-model mean (panel a). Panels d through i show different scenarios. Numbers above each map are correlation
coefficients between the absolute value of the change relative to 1995-2015 with the 1995-2015 anomaly map relative to the
pre-industrial era in panel c, except the red number at the top of panel b that is the correlation coefficient with this panel and
panel a.

The multi-model mean sink anomalies for two future periods, 2040-2060 and 2080-2100, show how the sink is
projected to evolve, relative to 1995-2015, according to time and choice of emission scenario (Fig. 1d-i). The
regional patterns show mostly positive anomalies at mid-century. Towards the end of the century, however,
negative anomalies are expected in ssp126, as emissions turn negative in the late-century in this scenario. The late-
century anomalies are predominantly positive in ssp585 which corresponds to the highest emission scenario, while

234 ssp245 is somewhere in between, with regions of positive and negative anomalies. The globally integrated ocean

235 carbon uptake rates are summarized in Table 1.

236

237

238
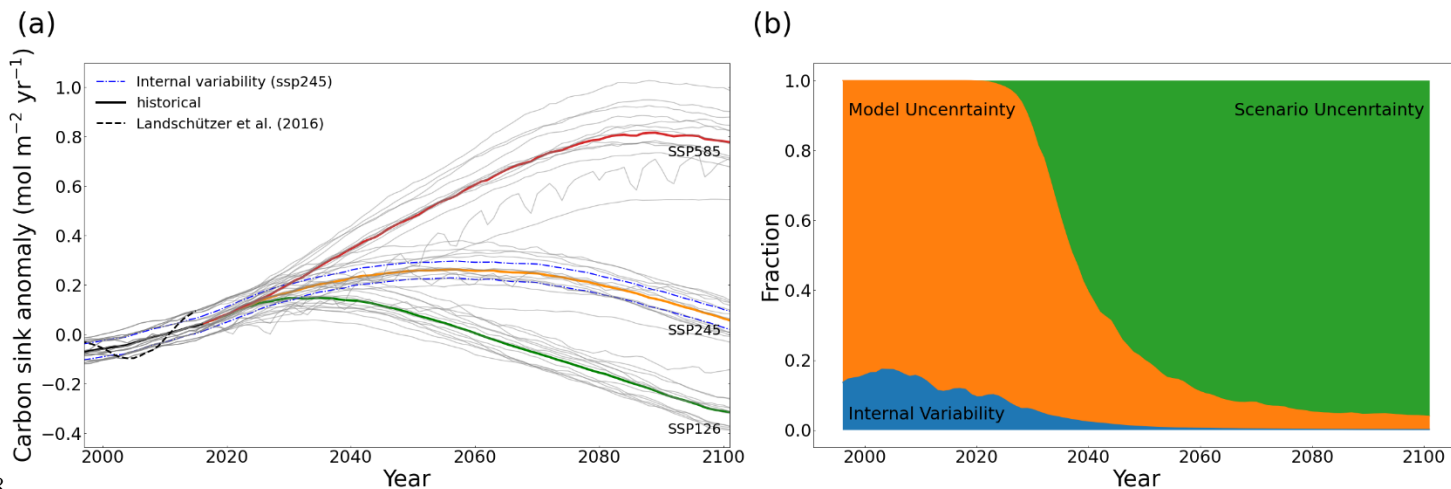
239 **Figure 2**- (a) Thick lines are multi-model means of the global mean ocean carbon sink anomaly timeseries relative to 1995-

240 2015. Individual models averaged for the means are plotted as thin grey lines in the background. The black dashed line

241 shows the Landschützer et al. (2016) SOM-FFN product. The blue dashed lines show internal variability for ssp245. (b)

242 Timeseries showing the breakdown of uncertainty to different sources with time for the global ocean carbon sink anomaly.

243 The internal and model uncertainty are averaged for different scenarios.

244

245

246

247

248

249

250

251

252

253

254

255

756

	Scenario	1995-2020	2020-2040	2040-2060	2060-2080	2080-2100
Anomaly (range)	ssp126 ssp245 ssp585	0.00 (-0.06 – 0.06)	0.13 (0.05 – 0.21) 0.17 (0.08 – 0.24) 0.22 (0.11 - 0.30)	0.07 (-0.02 – 0.16) 0.25 (0.11 – 0.36) 0.49 (0.29 – 0.62)	-0.08 (-0.14 - -0.01) 0.23 (0.09 – 0.33) 0.71 (0.45 – 0.90)	-0.24 (-0.3 - -0.12) 0.13 (0.02 – 0.21) 0.80 (0.54 – 1.00)
Internal (model) Uncertainty	ssp126 ssp245 ssp585 Average	0.032 (0.08) 0.032 (0.08)	0.033 (0.11) 0.032 (0.11) 0.033 (0.13) 0.033 (0.12)	0.034 (0.11) 0.034 (0.14) 0.037 (0.2) 0.035 (0.16)	0.035 (0.10) 0.037 (0.14) 0.045 (0.26) 0.039 (0.18)	0.036 (0.11) 0.036 (0.12) 0.043 (0.27) 0.038 (0.18)

757

758 **Table 1**- CMIP6 multi-model mean globally averaged carbon sink anomalies (with ranges within the 20-yr period in

759 parentheses) relative to the 1995-2015 mean (in mol-C m^{-2} yr^{-1}) and Internal variability (with model uncertainty in

760 parentheses) for the globally averaged ocean carbon sink anomalies for the three scenarios and the average values across

761 scenarios.

762

763

764 The trends in ocean carbon sink anomalies over 1995-2015 are statistically consistent between the CMIP6 multi-

765 model ensemble mean and the Landschützer et al. (2016) observation-based data product (Fig. 2-a), based on the

766 test from Santer et al. (2008). However, the SOM-FFN based time-series shows a larger multi-decadal variability

767 than seen in individual model realizations, and is larger than the range of internal variability estimated from the

768 CanESM5 SMILE. The difference could be due to either overestimation of internal variability by the SOM-FFN

769 method, or underestimation of the internal variability in the models. Given that on regional scales the SOM-FFN

770 data is within the range of internal variability projected by the CMIP6 large-ensemble of CanESM5 (see Sect. 3.3),

771 and that there are significant gaps in the spatial and temporal sampling that underlies the Landschützer et al. (2016)

772 estimate, it seems plausible that the discrepancy is largely due to overestimation of internal variability on the global

73   scale by the SOM-FFN technique. This is consistent with the findings of Gloege et al. (2021), which showed that,

74   globally, the magnitude of decadal variability is overestimated by 21% by the SOM-FFN technique, attributed to

75   the amount of data filling.

76

77   On the global scale, model uncertainty is the dominant source of uncertainty in the historical period, but scenario

78   uncertainty comes to dominate later (Fig. 2b). Over the 1995-2020 period, model uncertainty explains around 85%

79   of the total uncertainty. Scenario uncertainty becomes the dominant source after 2040, explaining almost 40% of

80   the total uncertainty at that time and more than 90% by the end of the century. Internal variability explains 15% at

81   the start of the century but only around 1% by the end. It is worth mentioning that the decreased shares associated

82   with model and internal variability do not mean that model or internal variability decrease in an absolute sense;

83   rather, their importance relative to scenario uncertainty declines. Internal and model uncertainty of the global

84   carbon sink change with time, based on the scenario (Table 2); high emission scenarios such as ssp585 show a

85   larger change for both internal and model uncertainty. When averaged for the three scenarios, a constant absolute

86   increase in both model and internal variability is seen through the century until 2080-2100 when the values either

87   do not change or decrease slightly (Table 1).

88

89

90   3.2 Dependence of the sources of uncertainty on spatial scale

91   It is generally accepted that uncertainty and, most importantly, internal variability grow larger as the averaging

92   (integration) scale gets finer, because on larger scales the variability is averaged out. Lovenduski et al. (2016)

93   showed this scale dependence by comparing an area covering the California Current System with the global ocean.

94   Here, we provide a continuous view of change in variability across scales from the global to grid scale, by

95   measuring how variability changes relative to scale on average (Fig. 3). At the global scale, the dominant source

96   of uncertainty is scenario uncertainty, followed by model and internal variability respectively, consistent with Fig.

97   2b. However, as the averaging (integration) scale gets finer, model and internal variability grow rapidly, while

98   scenario uncertainty only grows slightly on average (over all regions of this size). At an averaging (integration)

99   scale with an area finer than 75 million km^2 (on average around the globe), model uncertainty becomes the dominant

00   source of uncertainty, and at a scale finer than 3 million km^2, internal variability becomes larger than scenario

01   uncertainty. However, while this holds true on average over the globe, scale dependence can vary in its nature

02   depending on the particular region being sampled.

03

'04
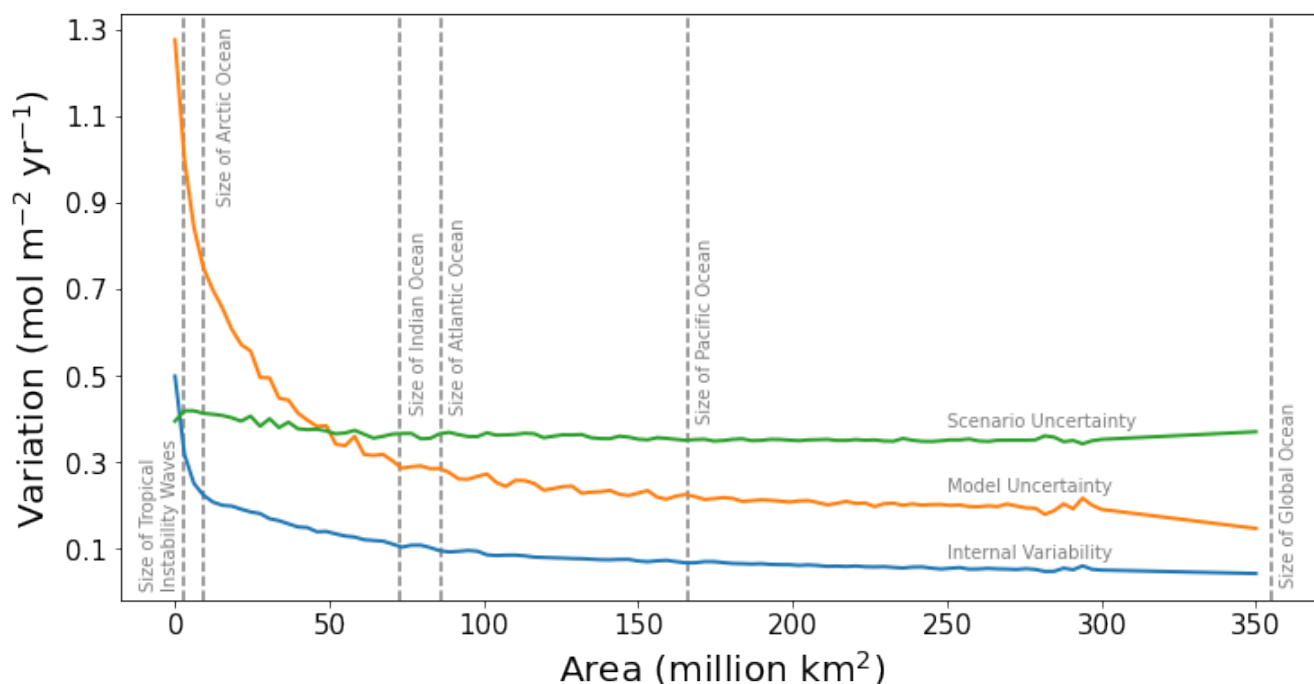
'05

'06 **Figure 3**- Sources of uncertainty versus area of averaging. Internal variability is based on ssp245 year 2050 of all CanESM5

'07 members. Scenario uncertainty is based on all scenarios of the 13 models at year 2050 and model uncertainty is the corrected

'08 standard deviation of our 13 models at year 2050 of ssp245. The values of uncertainties are averaged over all different

'09 rectangular areas of each size that can scan the globe. Dashed lines indicate the size of the averaging window and not a

'10 specific location.

'11

'12 3.3 Regional Analysis

'13 The findings of the globally averaged scale dependence analysis were tested by repeating the uncertainty

'14 breakdown for two specific regions: one between 20°- 60° N in the North East Pacific (NE Pacific) between 130°-

'15 160° W and one in the North West Atlantic (NW Atlantic) between 40°- 70° W at the same latitude. The NW

'16 Atlantic region represents a hotspot while the NE Pacific region is more typical of quiescent ocean regions. By

'17 quiescent ocean regions we refer to regions where strong stratification limits the vertical transport of carbon by

'18 isolating the surface.

'19

'20 The variation across scenarios is at all times smaller than internal variability in the NE Pacific (Fig. 4a). This

'21 suggests both that it will be difficult to robustly detect any human induced changes in observations of the NEP

22   carbon sink, and that potential future differences relating to choice of mitigation scenarios will not be readily

23   apparent in the NE Pacific carbon flux. This is true even for the high emission scenarios, because the anomalies

24   are small regardless of scenario (Table 2). In the NW Atlantic however, the deviation across scenarios becomes

25   larger than the internal variability in the early 2060s (Fig. 4c). The response of the region to climate change is

26   dependent on the scenario (Table 2), or, in other words, the amount of carbon dioxide in the atmosphere. This is

27   because the NW Atlantic is a hotspot where the air-sea flux actively responds to the atmospheric CO_2 concentration.

28   The trend of the CMIP6 multi-model time-series over the historical period is statistically consistent (Santer et al.,

29   2008) with that of the observation-based SOM-FFN product, and the multi-decadal variability is within the range

30   of internal variability measured by the CanESM5 large-ensemble in both regions. We note that both of these regions

31   are relatively well sampled, which may lead to more robust estimates of multi-decadal variability in the

32   Landschützer et al. (2016) dataset, and better agreement with the models than seen at the global scale.

33

34   Fractional estimates of each source of uncertainty vary with time and have different patterns for these two regions.

35   Internal variability and model uncertainty in the NE Pacific and NW Atlantic are larger by an order of magnitude

36   than at the global scale (Table 2). Over the period 1995-2020, model uncertainty is the dominant source of

37   uncertainty in both the NE Pacific and NW Atlantic (80-90%), while the remainder is internal variability (Fig. 4bd).

38   Internal variability explains around 25-30% of the total uncertainty in the NE Pacific throughout the century. In the

39   NW Atlantic however, its share drops to 15% by the end of the century. The share attributable to internal variability

40   is much larger during the 21st century in both regions compared to the global scale. Internal variability is larger in

41   the NW Atlantic in an absolute sense (Table 2), but its share of the total uncertainty is larger in NE Pacific (Fig.

42   4b). Overall, internal variability averaged over the scenarios shows a small increase, but no clear trend in time in

43   both regions until the 2080-2100 period where it decreases, consistent with the global estimates. The dependence

44   of internal variability on the scenario is an interesting result which requires further evaluations to understand the

45   degree of dependence and the driving mechanisms of such changes with time based on scenario. We showed earlier

46   that the NE Pacific scenarios do not differ much as the region is not a hotspot region - scenario uncertainty explains

47   less than 20% of the total uncertainty at the end of the century in the NE Pacific. In the NW Atlantic, scenario

48   uncertainty grows larger with time, becoming 45-50% of total uncertainty by the end of the century. In both

49   regions, model uncertainty is the dominant source of uncertainty in all years.

50
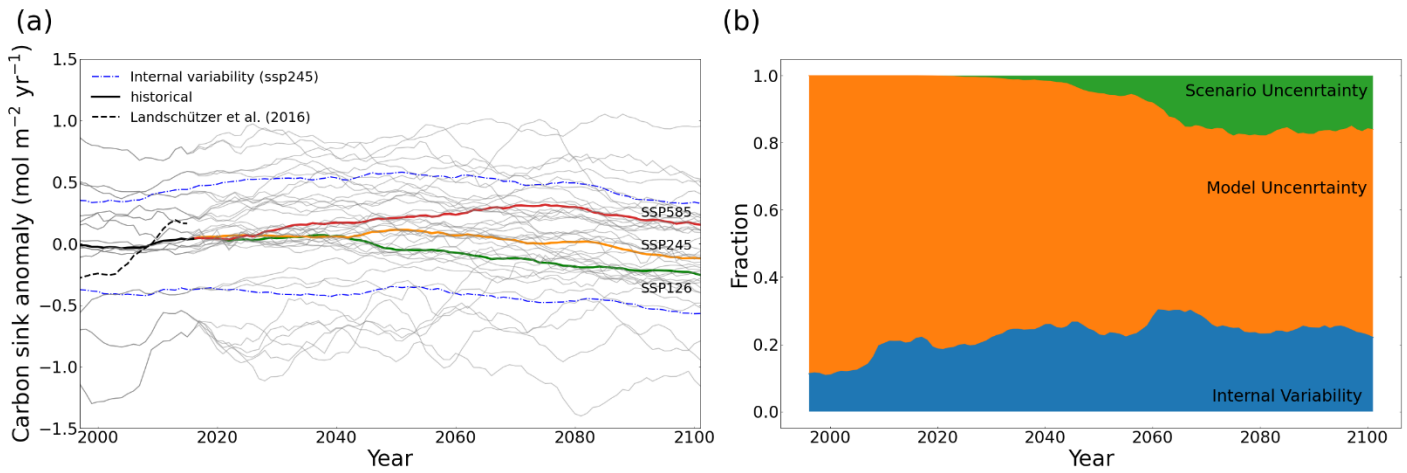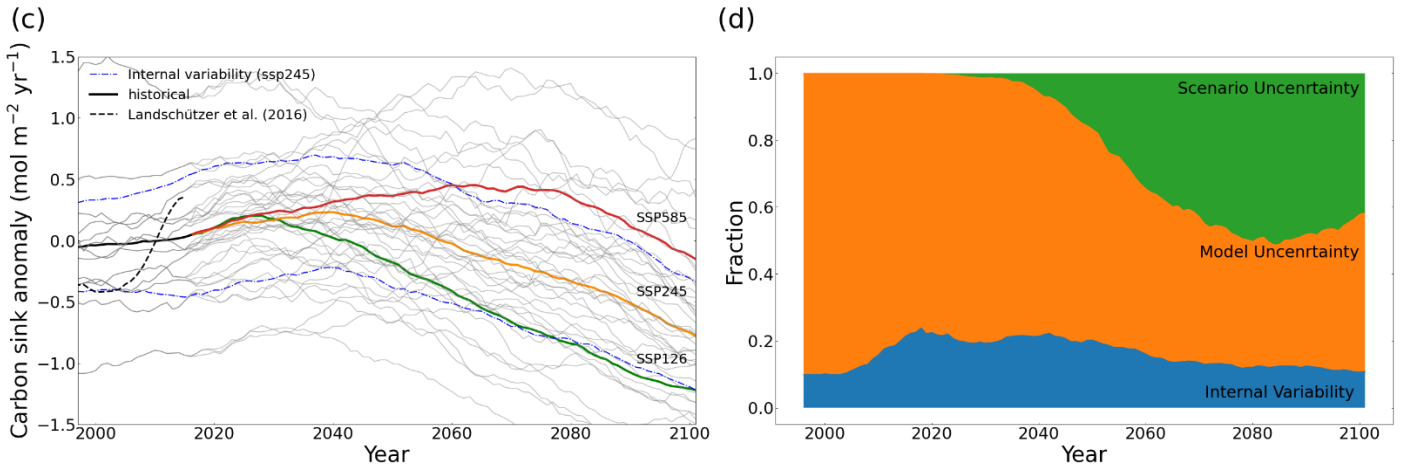
Figure 4- (a), (c) Thick lines are multi-model mean timeseries of anomalies relative to the 1995-2015 mean. All model time-series averaged for the means are plotted in grey lines in the background. The black dashed line shows the Landschützer et al. (2016) SOM-FFN product. The blue dashed line shows the internal variability measured as two times the standard deviation across all 50 members of CanESM5 only for ssp245 here. (b), (d) time-series showing the breakdown of uncertainty to different sources with time. The internal and model uncertainty are averaged for different scenarios. (a), (b) NE Pacific (40-60 °N, 130 -160 °W). (c), (d) NW Atlantic (40 - 60 °N, 40 -70 °W)

65

		Scenario	1995-2020	2020-2040	2040-2060	2060-2080	2080-2100
North East Pacific	Anomaly (range)	ssp126 ssp245 ssp585	0.00 (-0.98 – 0.76)	0.05 (-0.91 – 0.86) 0.06 (-0.86 – 0.83) 0.11 (-0.73 - 0.79)	0.03 (-0.86 – 0.62) 0.09 (-0.74 – 0.81) 0.21 (-0.61 – 0.86)	-0.13 (-1.1 – 0.58) 0.03 (-0.65 – 0.60) 0.29 (0.22 – 0.94)	-0.21 (-1.18 - 0.60) 0.06 (-0.70 – 0.53) 0.2 (-0.25 – 0.98)
	Internal (model) Uncertainty	ssp126 ssp245 ssp585 Average	0.39 (0.90) 0.39 (0.90)	0.47 (0.87) 0.46 (0.87) 0.45 (0.81) 0.46 (0.86)	0.43 (0.74) 0.47 (0.81) 0.47 (0.745) 0.46 (0.77)	0.40 (0.81) 0.48 (0.64) 0.58 (0.55) 0.47 (0.70)	0.39 (0.83) 0.45 (0.53) 0.44 (0.57) 0.43(0.67)
North West Atlantic	Anomaly (range)	ssp126 ssp245 ssp585	0.00 (-0.97 – 1.31)	0.13 (-0.77 – 1.21) 0.18 (-0.78 – 1.23) 0.23 (-0.70 – 1.20)	-0.20 (-1.03 – 0.56) 0.10 (-0.68 – 0.80) 0.38 (-0.41 – 1.12)	-0.66 (-1.45 – -0.11) -0.20 (-0.97 – 0.50) 0.41 (-0.27 – 1.29)	-1.00 (-1.80 - -0.56) -0.54 (-1.22 – 0.07) 0.10 (-0.70 – 0.96)
	Internal (model) Uncertainty	ssp126 ssp245 ssp585 Average	0.43 (1.02) 0.43 (1.02)	0.47 (0.91) 0.47 (0.96) 0.50 (0.90) 0.48 (0.93)	0.47 (0.79) 0.49 (0.82) 0.51 (0.94) 0.49 (0.87)	0.46 (0.78) 0.49 (0.80) 0.52 (1.00) 0.49 (0.88)	0.42 (0.80) 0.47 (0.79) 0.53 (1.00) 0.48 (0.88)

66

67 **Table 2-** CMIP6 multi-model mean sink anomalies (with ranges in parentheses) relative to 1995-2015 mean (in mol-C m^{-2}

68 yr^{-1}) and internal variability (with model uncertainty in parentheses) for the three scenarios and their average values in NE

69 Pacific and NW Atlantic.

770

771 The regional analysis shows that while uncertainty and its distribution among sources depends on the spatial scale

772 of integration, the specific location also matters. Regional patterns of uncertainty broken down by the source are

773 needed to clarify changes based on location. Consistent with the sink anomaly maps (Fig. 1), the regions that show

774 highest uncertainty for any of the sources in the future, are the same regions that show the largest uncertainties in

775 the historical period (Fig. 5). More importantly, the regions of largest future uptake uncertainty are highly correlated

776 with the historical regions of largest uptake, as shown by the pattern correlation coefficients above each panel. This

777 is a highly significant finding, because it suggests that knowledge of the modern day surface carbon flux anomaly

778 provides us with information about future uptake uncertainty.

779

780 The regions of high internal variability (eastern boundary upwelling regions, western boundary currents of the Gulf

781 Stream and Kuroshio, their extensions, and the Southern Ocean) are mostly within hotspots but are not confined to

782 them and do not include all of them. This lack of correspondence explains why the correlation coefficients are not

783 high for internal variability. An increase in internal variability with time is seen mostly in regions such as the

784 Southern Ocean, the Arctic Ocean, and boundaries of the gyre systems, while the rest of the ocean does not show

785 a clear change. The maps in Figure 5 are averaged over the three scenarios, which masks the changes to some

786 extent. However, we show in the Supplements (see section S2) that changes in the globally averaged internal

787 variability with time are different for different scenarios. Model uncertainty is consistently highest in the hotspot

788 regions, leading to stronger correlation with the anomaly maps of Fig. 1c. The model uncertainty is largest in the

789 Southern Ocean, where the complex time-evolving nature of the sink varies on all time-scales. The importance of

790 model uncertainty in the Southern Ocean provides a clear focal point for modelling centres to concentrate their

791 efforts in reducing projection uncertainty. Atmospheric teleconnections might play an important role in generating

792 the highly variable Southern Ocean carbon sink on decadal scales, and these are poorly constrained and represented

793 by models (Gruber et al. 2019).

794

795 Scenario uncertainty exhibits the largest change with time. This is by construction, meaning that scenarios are

796 designed to deviate from each other as time goes forward. Importantly, the correlation coefficients are highest

797 between scenario uncertainty and the current sink regions, indicating that the hotspot regions are the regions that

798 show the largest divergence among scenarios, and that the sink in most other regions does respond as strongly to

799 scenario differences. We showed an example of this earlier, where the timeseries of the multi-model signals for the

800 three scenarios did not emerge out of internal variability in the NE Pacific by 2100, whereas they did for the hotspot

·01   region of the NW Atlantic. This shows that, in these active hotspot regions, the sink evolves according to

·02   atmosphere CO_2 concentration via ocean processes that keep the surface ocean CO_2 out of equilibrium with the

·03   atmosphere. These uncertainties are central to the ability to detect human induced trends in observations of the

·04   surface ocean carbon flux, to which we now turn.

·05
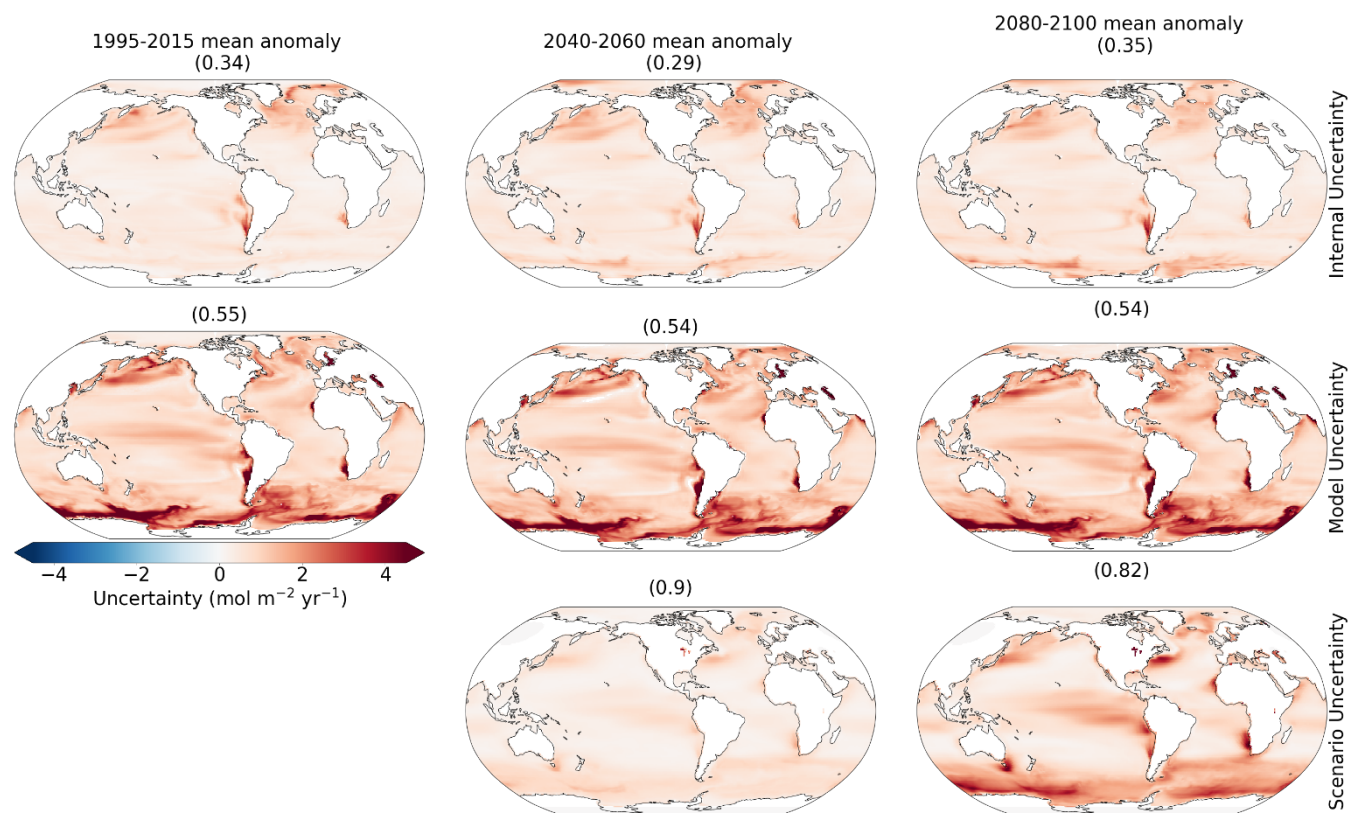
·06

·07   **Figure 5-** Sources of uncertainty averaged over the 20 year mean periods. The rows represent different sources as

·08   explained in the methods section at each grid cell. Columns represent different times: the recent (1995-2015), mid-

·09   century (2040-2060), and late-century (2080-2100) anomalies relative to the 1995-2015 mean. The numbers are

·10   correlation coefficients of each map with the 1995-2015 mean anomaly relative to the 1850-1900 mean (Fig. 1c).

·11

·12   3.4 Detectability

·13   Detectability refers to the ability to robustly identify a forced signal, above and beyond the noise induced by internal

·14   climate variability. Understanding the regional differences, timescales, and scenario dependence in the detectability

·15   of human induced trends in the ocean surface carbon flux is important for informing observational strategies that

·16   aim to measure these changes.

·17

·18   We measure the detectability of the CMIP6 multi-model ensemble mean ocean surface carbon flux anomaly using

·19   the time of emergence at each grid point. We use this finest scale as it is the most applicable to observational

·20   communities for sampling. The time of emergence is defined as the point at which the forced signal, given by the

·21   multi-model ensemble mean flux anomaly, relative to 1995-2015, emerges from internal variability, given by the

·22   CanESM5 SMILE.

·23

·24   The signal in human induced surface ocean carbon flux emerges beyond the internal variability earlier in the hotspot

·25   regions than anywhere else. This is evident in the Equatorial Pacific, Southern Ocean, the western boundary

·26   currents of the gyre systems, and their extensions (Fig. 6). The fixed inactive regions, such as the centres of the

·27   mid-latitude gyre systems and the NE Pacific, show late emergence times and, in some cases, no detectability of

·28   the signal in any of the scenarios by 2100. This is consistent with the results from Sect. 3.3, in which we showed

·29   that internal variability is a significant source throughout the century in the NE Pacific, with scenarios never

·30   emerging out of the range of internal variability (Fig. 4a,b). This result argues for focusing observational efforts on

·31   the hotspot regions in order to detect human influence on the ocean carbon sink. Meanwhile, they imply that

·32   observational timeseries in quiescent regions, such as Ocean Station Papa in the NE Pacific, need to interpret any

·33   observed trends with care, since internal variability tends to dominate over human induced trends.

·34

·35

·36
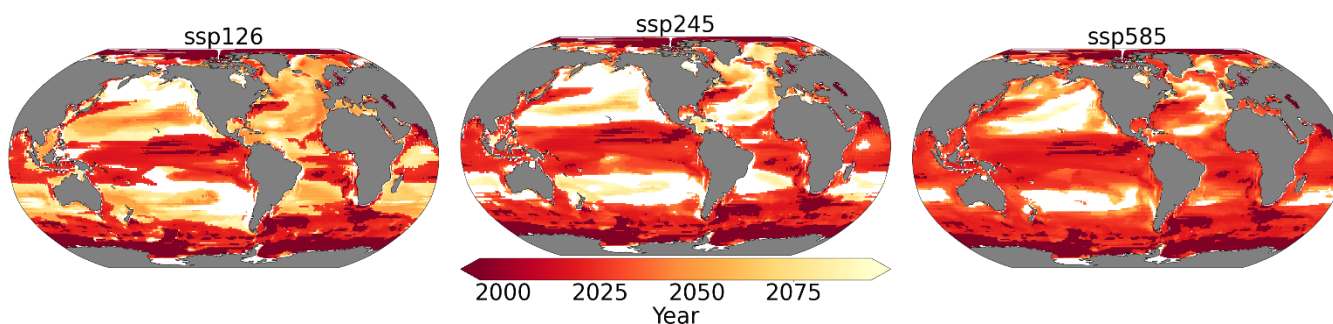
·37

·38   **Figure 6-** Time of emergence of the multi-model mean anomaly under different scenarios. White regions indicate

·39   where the anthropogenic signal cannot be detected even towards the end of the century.

40

41 Previous studies have largely presented a single time of emergence; however, the time of emergence strongly

42 depends on the future scenario. The time of emergence is earliest on average over the global ocean in ssp585, while

43 it is later in ssp245, and later still in ssp126. The earlier times of emergence are largely due to the stronger signal

44 in ssp585, and weaker in ssp245 and ssp126 (Fig. 2-a), consistent with the imposed changes in atmospheric CO_2

45 concentration. The exceptions are quiescent regions that show earlier detectability for ssp126 compared to other

46 scenarios; these exceptions are associated with larger (but negative) anomalies in the latter half of the century under

47 ssp126 which has negative emissions (compare panels d-f, and g-i on Fig. 1). Internal variability does evolve

48 somewhat differently for each scenario, but this is secondary (Fig. B2). Our results suggest that under the rapidly

49 rising atmospheric CO_2 concentrations seen in ssp585, the human signal in the ocean carbon sink will be detectable

50 across much of the global ocean over the coming few decades. However, under strong mitigation scenarios, such

51 as ssp126, early emergence will only occur in isolated regions.

52 **4. Conclusions**

53 Ocean carbon uptake as a result of increasing atmospheric CO_2 concentration occurs mostly in a few hotspot

54 regions. We analyze the results from the CMIP6 multi-model mean for the current state of the ocean (1995-2015),

55 and the middle (2040-2060) and late (2080-2100) 21st century relative to the current state for three scenarios. We

56 show that future changes in the sink mostly take place within the same historical hotspot regions. This result implies

57 that known regions of high historical uptake, including the North Atlantic and Southern Ocean, are the same regions

58 to prioritize for observing the future evolution of the sink.

59

60 We show that the CMIP6 multi-model mean provides a consistent estimate of the spatial patterns of the sink, and

61 the trend in the sink (globally), compared to the observation-based data product dataset of Landschützer et al.

62 (2016). These results suggest the CMIP6 models are valid tools for understanding the past and future evolution of

63 the ocean carbon sink, particularly at broad spatial scales. A notable area of disagreement is that the Landschützer

64 et al. (2016) data shows larger decadal variability at the global scale than seen in any CMIP6 model. We argue the

65 overestimation of internal variability by this dataset is a plausible explanation, since at the regional scale, there is

66 no such disagreement. This is in agreement with Gloege et al. (2021) who showed that the SOM-FFN method

67 overestimates the magnitude of decadal variability by 21% on the global scale.

68

769   We have shown that the magnitude of uncertainty and its partitioning among different sources differs with scale
770   and location. On the global scale, scenario uncertainty is the largest source of uncertainty followed by model
771   uncertainty and internal variability. However, as the scales of integration (averaging) get finer, model and internal
772   variability become the dominant sources, respectively. Testing the results on two ocean basins of about the same
773   size, one in the NE Pacific and one in the NW Atlantic shows that - while consistent with the results of the scale
774   dependence analysis - the relative importance of the sources of uncertainty also differs with location. Notably, in
775   hotspot regions, such as the NW Atlantic, scenario uncertainty is large, whereas in more quiescent regions, such as
776   the NE Pacific, internal variability is more significant. The dependence of internal variability on the scenario with
777   time is another interesting finding that could be the subject of future studies for a better understanding of the driving
778   mechanism and the degree of dependence on the future emissions and/or concentrations.

779

780   The patterns of high future CO_2 uptake uncertainty are highly correlated with the patterns of historical uptake. The
781   correlation coefficients are highest for scenario uncertainty, indicating that the hotspot regions have the potential
782   for the sink to evolve according to the atmospheric CO_2 concentration, while the rest of the ocean basins do not
783   respond strongly to changes in atmospheric CO_2 represented by the different scenarios. Our results here are
784   significant in that they show that regions of future uncertainty are largely associated with known regions of
785   significant historical uptake.

786

787   Patterns seen in the time-of-emergence have implications for planning observational campaigns for detection of a
788   signal. Our results show that there should be caution taken in interpreting the observed changes in regions such as
789   NE Pacific (where active sampling is being done) associated with the late time of emergence of the signal from the
790   decadal (internal) variations. On the other hand, regions such as the Equatorial Pacific, the Gulf Stream and
791   Kuroshio and their extensions, and the Southern Ocean, should be the focus of consistent and expanded sampling
792   for detection of the forced signal. Additionally, the patterns in sources of uncertainty show that model uncertainty
793   is largest in the Southern Ocean, consistent with previous studies. The sink in the Southern Ocean is driven by
794   complex mechanisms involving coupled ocean-atmosphere-ice interactions that require better representation in
795   ocean biogeochemical models. If we wish to constrain and reduce future uncertainties in the ocean carbon sink, our
796   results provide a motivation to focus modelling as well as observational efforts on the known hotspot regions of
797   historical uptake.

798

Data Availability

The data used in this study is part of the World Climate Research Programme's (WCRP) 6th Coupled Model Intercomparison Project (CMIP6) open access data. For details on accessibility see section S1 in the Supplements. The SOM-FFN data (Landschützer et al., 2017) from Landschützer (2016) can be accessed through the National Oceanographic Data Center (NODC, https://www.nodc.noaa.gov/archive/arc0105/0160558/3.3/data/0-data/) operated by the National Oceanic and Atmospheric Administration (NOAA) of the U.S. Department of Commerce.

Author Contribution

Parsa Gooya conducted the formal analysis, visualization, and original draft preparation. Conceptualization, and methodology development and validation were a collaboration of the three authors, mainly developed by Parsa Gooya with contributions from Neil Swart in development, validation, and revision and Roberta Hamme in validation and revision. Neil Swart and Roberta Hamme provided supervision and reviewing and editing of the manuscript and methodology. Funding acquisition was carried out by Roberta Hamme.

Competing of interest

The authors declare that they have no conflict of interest.

Acknowledgments

This work was supported by the Marine Carbon Sink project, funded by the Natural Sciences and Engineering Research Council of Canada through the Advancing Climate Change Science in Canada program. We thank Jim Christian for helpful suggestions on a draft of the manuscript.

References

Ciais, P. and Sabine, C.: Carbon and other biogeochemical cycles, in Climate Change 2013: The Physical Science Basis. Contribution of Working Group I to the Fifth Assessment Report of the Intergovernmental Panel on Climate Change. Cambridge Univ. Press, 2013.

Eyring, V., Bony, S., Meehl, G. A., Senior, C. A., Stevens, B., Stouffer, R. J., and Taylor, K. E.: Overview of the Coupled Model Intercomparison Project Phase 6 (CMIP6) experimental design and organization, Geosci. Model Dev., 9, 1937–1958, https://doi.org/10.5194/gmd-9-1937-2016, 2016.

Friedlingstein, P., Jones, M. W., O'Sullivan, M., Andrew, R. M., Bakker, D. C. E., Hauck, J., Le Quéré, C., Peters, G. P., Peters, W., Pongratz, J., Sitch, S., Canadell, J. G., Ciais, P., Jackson, R. B., Alin, S. R., Anthoni, P., Bates, N. R., Becker, M., Bellouin, N., Bopp, L., Chau, T. T. T., Chevallier, F., Chini, L. P., Cronin, M., Currie, K. I., Decharme, B., Djeutchouang, L., Dou, X., Evans, W., Feely, R. A., Feng, L., Gasser, T., Gilfillan, D., Gkritzalis, T., Grassi, G., Gregor, L., Gruber, N., Gürses, Ö., Harris, I., Houghton, R. A., Hurtt, G. C., Iida, Y., Ilyina, T., Luijkx, I. T., Jain, A. K., Jones, S. D., Kato, E., Kennedy, D., Klein Goldewijk, K., Knauer, J., Korsbakken, J. I., Körtzinger, A., Landschützer, P., Lauvset, S. K., Lefèvre, N., Lienert, S., Liu, J., Marland, G., McGuire, P. C., Melton, J. R., Munro, D. R., Nabel, J. E. M. S., Nakaoka, S.-I., Niwa, Y., Ono, T., Pierrot, D., Poulter, B., Rehder, G., Resplandy, L., Robertson, E., Rödenbeck, C., Rosan, T. M., Schwinger, J., Schwingshackl, C., Séférian, R., Sutton, A. J., Sweeney, C., Tanhua, T., Tans, P. P., Tian, H., Tilbrook, B., Tubiello, F., van der Werf, G., Vuichard, N., Wada, C., Wanninkhof, R., Watson, A., Willis, D., Wiltshire, A. J., Yuan, W., Yue, C., Yue, X., Zaehle, S., and Zeng, J.: Global Carbon Budget 2021, Earth Syst. Sci. Data Discuss. [preprint], https://doi.org/10.5194/essd-2021-386, in review, 2021.

Friedrich, T., Timmermann, A., Abe-Ouchi, A., Bates, N. R., Chikamoto, M. O., and Church, M. J.: Detecting regional anthropogenic trends in ocean acidification against natural variability. Nat. Clim. Change, 2, 167–171. doi: 10.1038/nclimate1372, 2012.

Frölicher, T. L., Sarmiento, J. L., Paynter, D. J., Dunne, J. P., Krasting, J. P., and Winton, M.: Dominance of the Southern Ocean in anthropogenic carbon and heat uptake in CMIP5 models, J. Clim., 28(2), 862– 886, 2014.

Gloege, L., McKinley, G. A., Landschützer, P., Fay, A. R., Frölicher, T. L., Fyfe, J. C., et al.: Quantifying errors in observationally based estimates of ocean carbon sink variability. Global Biogeochemical Cycles, 35, doi:10.1029/2020GB006788, 2021.

Gruber, N., Landschützer, P., and Lovenduski, N. S.: The Variable Southern Ocean Carbon Sink, Annual Review of Marine Science, 11:1, 159-186, 2019.

Gray, A. R., Johnson, K. S., Bushinsky, S. M., Riser, S. C., Russell, J.L., Wanninkhof, R., Williams, N. L., and Sarmiento, J. L.: Autonomous biogeochemical floats detect significant carbon dioxide outgassing in the high-latitude Southern Ocean, Geophys. Res. Lett., 45, 9049–57, 2018.

Hauck, J., Völker, C., Wolf-Gladrow, D. A., Laufkötter, C., Vogt, M., Aumont, O., Bopp, L., Buitenhuis, E. T., Doney, S. C., Dunne, J., Gruber, N., Hashioka, T., John, J., Le Quéré, C., Lima, I. D., Nakano, H., Séférian, R., Totterdell, I.: On the Southern Ocean CO_2 uptake and the role of the biological carbon pump in the 21st century, Global Biogeochem. Cycles, 29, 1451– 1470, doi:10.1002/2015GB005140, 2015.

Hawkins, E. and Sutton, R.: The potential to narrow uncertainty in regional climate predictions. Bull. Am. Meteorol. Soc., 90:1095, 2009.

Joos, F. and Spahni, R.: Rates of change in natural and anthropogenic radiative forcing over the past 20,000 years. Proceedings of the National Academy of Sciences of the United States of America, 105, 1425-30, 2008.

Kumar, D. and Ganguly, A. R.: Intercomparison of model response and internal variability across climate model ensembles, Clim. Dynam., 51, 207–219, https://doi.org/10.1007/s00382-017-3914-4, 2018.

Laufkötter, C., Vogt, M., Gruber, N., Aita-Noguchi, M., Aumont, O., Bopp, L., Buitenhuis, E., Doney, S. C., Dunne, J., Hashioka, T., Hauck, J., Hirata, T., John, J., Le Quéré, C., Lima, I. D., Nakano, H., Seferian, R., Totterdell, I., Vichi, M., and Völker, C.: Drivers and uncertainties of future global marine primary production in marine ecosystem models, Biogeosciences, 12, 6955–6984, https://doi.org/10.5194/bg-12-6955-2015, 2015.

Lovenduski, N. S., McKinley, G. A., Fay, A. R., Lindsay, K., and Long, M. C.: Partitioning uncertainty in ocean carbon uptake projections: Internal variability, emission scenario, and model structure, Global Biogeochem. Cycles, 30, 1276– 1287, 2016.

Lehner, F., Deser, C., Maher, N., Marotzke, J., Fischer, E. M., Brunner, L., Knutti, R., and Hawkins, E.: Partitioning climate projection uncertainty with multiple large ensembles and CMIP5/6, Earth Syst. Dynam., 11, 491–508, https://doi.org/10.5194/esd-11-491-2020, 2020.

Landschützer, P., Gruber, N., and Bakker, D. C. E.: Decadal variations and trends of the global ocean carbon sink, Global Biogeochem. Cycles, 30, 1396– 1417, doi:10.1002/2015GB005359, 2016.

Landschützer, P., Gruber N., and Bakker, D.C.E.: An updated observation-based global monthly gridded sea surface pCO_2 and air-sea CO_2 flux product from 1982 through 2015 and its monthly climatology (NCEI Accession 0160558), Version 2.2, NOAA National Centers for Environmental Information, Dataset, (2017-07-11).

Masson-Delmotte, V., P. Zhai, A. Pirani, S.L. Connors, C. Péan, S. Berger, N. Caud, Y. Chen, L. Goldfarb, M.I. Gomis, M. Huang, K. Leitzell, E. Lonnoy, J.B.R. Matthews, T.K. Maycock, T. Waterfield, O. Yelekçi, R. Yu, and B. Zhou (eds.): IPCC, 2021: Summary for Policymakers. In: Climate Change 2021, The Physical Science Basis. Contribution of Working Group I to the Sixth Assessment Report of the Intergovernmental Panel on Climate Change. In Press.

McKinley G. A., Pilcher D. J., Fay A. R., Lindsay K., Long M. C., and Lovenduski N. S.: Timescales for detection of trends in the ocean carbon sink. Nature, 530(7591), 469-72. doi: 10.1038/nature16958. PMID: 26911782, 2016.

Roy, T., L. Bopp, M. Gehlen, B. Schneider, P. Cadule, T. L. Frölicher, J. Segschneider, J. Tjiputra, C. Heinze, and F. Joos: Regional impacts of climate change and atmospheric CO_2 on future ocean carbon uptake: A multimodel linear feedback analysis, J. Clim., 24(9), 2300– 2318, 2011.

Santer, B.D., P.W. Thorne, L. Haimberger, K.E. Taylor, T.M.L. Wigley, J.R. Lanzante, S. Solomon, M. Free, P.J. Gleckler, P.D. Jones, T.R. Karl, S.A. Klein, C. Mears, D. Nychka, G.A. Schmidt, S.C. Sherwood, and F.J. Wentz: Consistency of modelled and observed temperature trends in the tropical troposphere. Int. J. Climatol., 28, 1703-1722, doi:10.1002/joc.1756, 2008.

Sutton AJ, Wanninkhof R, Sabine CL, Feely RA, Cronin MF, Weller RA. 2017. Variability and trends in surface seawater pCO_2 and CO_2 flux in the Pacific Ocean. *Geophys Res Lett* **44**(11): 5627–5636. doi: 10.1002/2017GL073814

Takahashi T, Sutherland SC, Feely RA, Wanninkhof R. 2006. Decadal change of the surface water pCO_2 in the North Pacific: A synthesis of 35 years of observations. *J Geophys Res* **111**(C7): C07S05. doi: 10.1029/2005JC003074

620

621 Tebaldi C. and Knutti R.: The use of the multimodel ensemble in probabilistic climate projections. Phil. Trans. R. Soc. A.,
622 365, 2053–2075, 2007.

623

624 Tjiputra, J. F., Olsen, A., Bopp, L., Lenton, A., Pfeil, B., Roy, T., Segschneider, J., Totterdell, I., and Heinze, C.: Long-term
625 surface pCO_2 trends from observations and models, Tellus B., 66, 23083, 2014.

626

627 Williams, N. L., Juranek, L. W., Feely, R. A., Russell, J. L., Johnson, K. S., and Hales, B.: Assessment of the carbonate
628 chemistry seasonal cycles in the Southern Ocean from persistent observational platforms. J. Geophys. Res. Oceans, 123,4833–
629 52, 2018.

630

631

632

633

634

635

636

637

638

639

640

641